Magnetic walls in the anisotropic XY-spin system in an oscillating magnetic field

Fujiwara, N; Tutu, H; Fujisaka, H

PHYSICAL REVIEW E **70**, 066132 (2004)

Magnetic walls in the anisotropic *XY*-spin system in an oscillating magnetic field

Naoya Fujiwara,* Hiroki Tutu,† and Hirokazu Fujisaka‡
Department of Applied Analysis and Complex Dynamical Systems, Graduate School of Informatics, Kyoto University, Kyoto 606-8501, Japan
(Received 17 May 2004; published 23 December 2004)

Wall structures associated with dynamic phase transitions in the anisotropic *XY*-spin system in a temporally oscillating magnetic field $h\cos(\Omega t)$ in a one-dimensional system are analyzed by using the time-dependent Ginzburg-Landau model. It is numerically confirmed that there exist two types of magnetic walls, i.e., the Néel and Bloch walls, and is found that the transition between the two walls can occur for changing h or Ω. The phase diagram for the stable regions of each wall is obtained by both numerical and analytical methods. Furthermore, the critical behavior of the modulus of the Bloch wall around the Néel-Bloch transition point is studied, and it is found that the transition can be either continuous or discontinuous with respect to h, depending on Ω.

DOI: 10.1103/PhysRevE.70.066132 PACS number(s): 64.60.−i, 05.45.−a, 75.60.−d

I. INTRODUCTION

Since the establishment of the linear response theory in the 1950s and nonequilibrium statistical mechanics in the 1960s, the frontier of statistical physics is extending to systems that are far from equilibrium. A magnetic system under a temporally oscillating field is one example of far-from-equilibrium systems. Since the 1990s, many studies with the mean field theoretical approach [1,2] and Monte Carlo simulations [3–6] as well as laboratory experiments [7–9] have been carried out to study responses of ferromagnetic systems to a temporally oscillating, strong magnetic force.

The mean field theoretical analysis made it clear that when the amplitude h of the oscillating magnetic field is kept strong enough, two types of magnetization cycle either with or without a certain symmetry in time are possible, depending on the frequency Ω of the applied field. When Ω is below a critical value Ω_c, the magnetization cycle is described as an oscillation with a temporal symmetry (symmetry-restoring oscillation, SRO), and beyond Ω_c it is described as an oscillation without such symmetry (symmetry-breaking oscillation, SBO). These characteristic oscillating states under oscillating magnetic field are called *dynamic phases* and such a transition between two phases under a change of either the amplitude or the frequency of the amplified field is called the *dynamic phase transition* (DPT) [4].

Furthermore, the Monte Carlo simulation of a two-dimensional (2D) Ising spin system below the critical temperature proved that for a fixed h the probability density of the magnetization averaged over one period of the oscillating field has one peak for $\Omega<\Omega_c$, and double peaks for $\Omega>\Omega_c$ therefore the transition is associated with the symmetry change of the magnetization cycle. In addition, a finite size scaling analysis proved that the DPT belongs to the same universality class as the phase transition of a kinetic Ising spin system in thermal equilibrium [3–6]. This fact was also confirmed by a Landau expansion near the transition point [10].

Recently, experimental studies of dynamic phase transitions in a Heisenberg-type ferromagnet with uniaxial anisotropy have been carried out [8,9]. Monte Carlo simulations of the Heisenberg spin system with uniaxial anisotropy in an oscillating magnetic field were carried out [11,12]. It was reported that when the magnetic field is applied to the non-easy axis of magnetization, magnetization perpendicular to the applied field is observed [12].

Very recently, in order to study the DPT in a multicomponent system from the mean field theoretical viewpoint, Yasui *et al.* studied the time-dependent Ginzburg-Landau (TDGL) equation

$$\dot{\psi}(\mathbf{r},t) = (T_c - T)\psi - |\psi|^2\psi + \gamma\psi^* + \nabla^2\psi + h\cos(\Omega t)(T < T_c) \tag{1.1}$$

corresponding to the anisotropic *XY*-spin system [13]. Here, $\psi(\mathbf{r},t)=X(\mathbf{r},t)+iY(\mathbf{r},t)$ is the complex order parameter, and X and Y are components of the coarse-grained *XY* spin ψ at the location $\mathbf{r}$ and time t. The parameter γ stands for the magnitude of the magnetic anisotropy, and for $\gamma>0(<0)$ the X (Y) axis corresponds to the magnetic easy axis. In the limit $|\gamma|\to\infty$, the above model is reduced to the Ising model, and it is identical to the isotropic *XY* model for $\gamma=0$. The fourth term implies the local ferromagnetic interaction. The last term represents the oscillating external force applied in the X direction, where h and Ω are, respectively, its amplitude and frequency.

With rescalings $\psi\to(T_c-T)^{1/2}\psi$, $t\to(T_c-T)^{-1}t$, $\nabla\to(T_c-T)^{1/2}\nabla$, $\gamma\to(T_c-T)\gamma$, $h\to(T_c-T)^{3/2}h$, $\Omega\to(T_c-T)\Omega$, the equation of motion (1.1) can be transformed into the dimensionless TDGL equation

$$\dot{\psi}(\mathbf{r},t) = \psi - |\psi|^2\psi + \gamma\psi^* + \nabla^2\psi + h\cos(\Omega t). \tag{1.2}$$

Noting that thermal noise does not play a crucial role in a strongly oscillating magnetic field, we have neglected the

*Electronic address: naoya@acs.i.kyoto-u.ac.jp
†Electronic address: tutu@acs.i.kyoto-u.ac.jp
‡Electronic address: fujisaka@i.kyoto-u.ac.jp

thermal noise in the basic dynamics. In the present paper, we consider the situation that the system forms a nearly 1D spatial structure, which is supposed to be along the z direction, in the spatial dimension above 1, and the time evolution can be described with the 1D version of Eq. (1.2), i.e.,

$$\dot{X}(z,t) = [1 + \gamma - (X^2 + Y^2)]X + \partial_z^2 X + h\cos(\Omega t),$$

$$\dot{Y}(z,t) = [1 - \gamma - (X^2 + Y^2)]Y + \partial_z^2 Y. \tag{1.3}$$

Recently, Yasui *et al.* analyzed the spatially uniform oscillation and clarified the possible types of oscillations, which are called the Ising-SRO, Ising-SBO, *XY*-SRO, and *XY*-SBO oscillations (for details, see Sec. II).

So far, many studies have been carried out for magnetic wall structures in ferromagnetic systems, and in the ordering process, the interactions among magnetic walls and the domain size distribution were studied using the TDGL equations [14–17]. It is known that in a perturbed parametrically driven, damped nonlinear Schrödinger equation, as the parameter is changed, a structural transition of the domain wall can occur, i.e., the Néel- (Ising-) Bloch transition exists [18]. Furthermore, the dynamical properties of the Bloch wall in an oscillating magnetic field have been studied for the sine-Gordon and Landau-Lifshitz equations, respectively [19,20]. However, no study on the change of symmetry and structures of walls associated with the dynamic phase transition has been carried out. The fundamental aim of the present paper is to clarify the wall structures and their dynamics associated with the dynamic phase transition in the anisotropic *XY*-spin system (1.3) in an oscillating magnetic field.

The present paper is organized as follows. Section II gives a brief review of the dynamic phase transition of the spatially uniform case of the anisotropic *XY*-spin system studied by Yasui *et al.* In Sec. III, wall structures in an oscillating magnetic field and their oscillatory characteristics are studied. The existence of the Néel-Bloch wall transition is also shown as either the amplitude or the frequency of the external field is changed. Section IV shows an analysis for the Néel-Bloch transition from the Fourier expansion approach. The result is compared with the numerically obtained one. In Sec. V, the h dependence of the Bloch wall modulus near the Néel-Bloch transition point is studied. The numerical result is shown in Sec. V A, and we develop the Fourier expansion theory of wall dynamics in Sec. V B. A summary and concluding remarks are given in the last section.

II. OSCILLATION AND PHASE DIAGRAMS OF UNIFORM OSCILLATIONS

In this section we give a brief review of the spatially uniform oscillations of the TDGL equation (1.3), reported in Ref. [13]. The uniform solutions of Eq. (1.3) are limit cycles, which can be classified by two types of symmetries.

First, if $\psi(t) = X(t) + iY(t)$ is a solution of Eq. (1.3), then

$$\hat{\psi}(t) = -X(t + T/2) + iY(t + T/2) \tag{2.1}$$

($T = 2\pi/\Omega$ is the period of the magnetic field) is also a solution of Eq. (1.3), because Eq. (1.3) is invariant under the transformation $t \to t + T/2$, $X \to -X$, and $Y \to Y$. Owing to this symmetry, Eq. (1.3) always has a solution that satisfies $\psi(t) = \hat{\psi}(t)$, i.e.,

$$X(t) = -X(t + T/2), \tag{2.2}$$

$$Y(t) = Y(t + T/2). \tag{2.3}$$

We call this type of solution the symmetry-restoring oscillation and a solution which does not satisfy this relation the symmetry-breaking oscillation. In the SRO, the time average of the X component over one period satisfies

$$\frac{1}{T}\int_0^T X(t)dt = 0. \tag{2.4}$$

There is also another kind of symmetry. If $\psi(t) = X(t) + iY(t)$ is a solution of Eq. (1.3),

$$\tilde{\psi}(t) = X(t) - iY(t) \tag{2.5}$$

is also a solution of Eq. (1.3). Equation (1.3) always has a trivial solution that satisfies

$$\psi(t) = \tilde{\psi}(t), \text{ i.e., } Y(t) = 0. \tag{2.6}$$

We call this type of oscillation the *Ising oscillation* because the oscillator has only the X component. On the other hand, any solution such that $Y(t) \neq 0$ is called the *XY oscillation*.

In terms of these two types of symmetries, we can classify the uniform solutions into four types, Ising-SRO, Ising-SBO, *XY*-SRO, and *XY*-SBO. These orbits have different types of symmetry and are called the dynamic phases, which are shown in Fig. 1. According to the symmetries described above, two stable limit cycles coexist in the Ising-SBO and *XY*-SRO phases and four stable limit cycles in the *XY*-SBO phase. The symmetry of the uniform solution changes as the amplitude or the frequency of the magnetic field is changed. This phenomenon is called the dynamic phase transition.

The phase diagram of the uniform solutions is obtained by applying the Floquet analysis. Let $\psi(t)$ be a uniform solution and $\psi_0(t) = X_0(t) + iY_0(t)$ be one of the limit cycles. The linearized equation for the deviation from the limit cycle solution $\delta\psi(t) = \psi(t) - \psi_0(t) = x(t) + iy(t)$ is derived as

$$\frac{d}{dt}\begin{pmatrix} x(t) \\ y(t) \end{pmatrix} = \hat{G}(t)\begin{pmatrix} x(t) \\ y(t) \end{pmatrix}, \tag{2.7}$$

$$\hat{G}(t) = \begin{pmatrix} 1 + \gamma - 3X_0(t)^2 - Y_0(t)^2 & -2X_0(t)Y_0(t) \\ -2X_0(t)Y_0(t) & 1 - \gamma - X_0(t)^2 - 3Y_0(t)^2 \end{pmatrix}, \tag{2.8}$$

where $\hat{G}(t)$ is the period-T matrix. We define the time evolution operator $\hat{U}(t)$ by $(x(t), y(t))^T = \hat{U}(t)(x(0), y(0))^T$ with the initial condition $\hat{U}(0) = \hat{1}$, $\hat{1}$ being the 2×2 unit matrix. The time evolution of $\hat{U}(t)$ is described by $d\hat{U}(t)/dt = \hat{G}(t)\hat{U}(t)$, which can be written in the form

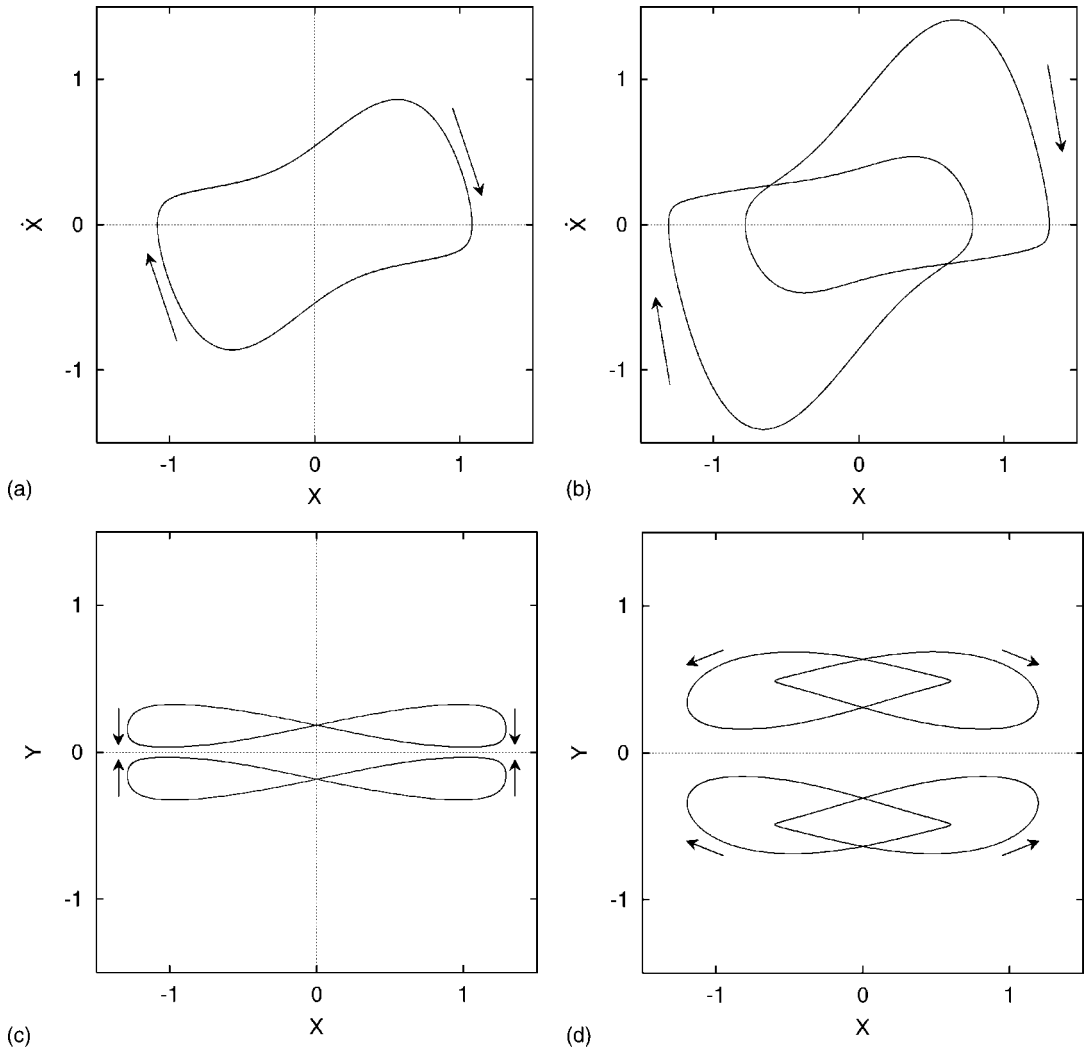

FIG. 1. The limit cycle attractor(s) in the four dynamic phases: (a) Ising-SRO, (b) Ising-SBO, (c) *XY*-SRO, and (d) *XY*-SBO. The horizontal and vertical axes represent X and $\dot{X}$ components in (a) and (b) (Ising phases), and X and Y components in (c) and (d) (*XY* phases), respectively. The other phases except the Ising-SRO phase have plural coexisting stable limit cycles.

$$\hat{U}(t) = \hat{Q}(t)e^{t\hat{\Lambda}}, \tag{2.9}$$

where $\hat{\Lambda}$ is the Floquet matrix defined by

$$\hat{U}(T) = e^{T\hat{\Lambda}}, \tag{2.10}$$

and $\hat{Q}(t)$ is a period-T matrix of t. At the DPT point, the maximum eigenvalue of the matrix $\hat{\Lambda}$ vanishes.

Typical phase diagrams of the uniform solutions, as well as the magnetic wall solutions, obtained by the Floquet analysis are shown in Figs. 2–4 for (1) $\gamma > 1/2$ (Fig. 2), (2) $0 < \gamma < 1/2$ (Fig. 3), (3) $\gamma < 0$ (Fig. 4). It should be noted for $\gamma > 1/2$ that only the Ising-SRO and Ising-SBO phases are observed. For $0 < \gamma < 1/2$, the four types of dynamic phases shown in Fig. 1 are present. One should note that the *XY*-SBO phase is observed in a small region between the *XY*-SRO and Ising-SBO phases. For $\gamma < 0$, the Ising-SRO and *XY*-SRO phases are observed. These phase diagrams also indicate several types of magnetic wall structures which exist for certain parameter ranges in each phase of the uniform solutions. The magnetic walls will be dealt in Sec. III.

The existence of the DPT is intuitively interpreted as follows. For $0 < \gamma < 1/2$, if h is fixed beyond a threshold value and Ω is changed, we observe four types of dynamic phases. When Ω is small enough, the time scale of spin relaxation is much shorter than the period of the oscillating magnetic field. In this situation a spin follows the temporal variation of the magnetic field, and as a result, the Ising-SRO phase is observed. As Ω is increased, the time scale of spin relaxation becomes comparable to that of the magnetic field, and the spin cannot follow the variation of the magnetic field. As a result, the spin dynamics has the Y component, and its X component which measures the extent of the synchronization to the magnetic field is reduced. That is the intuitive reason why we observe the *XY*-type oscillation even when the magnetic field is applied along the easy (X) axis. As Ω is increased, the effect of the magnetic field becomes smaller because the time scale of the magnetic field is much shorter than that of spin relaxation, the magnetic field is effectively averaged and makes a weak contribution to the spin dynam-

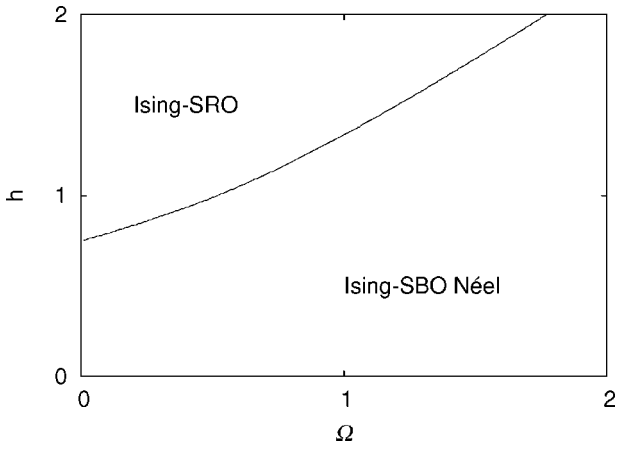

FIG. 2. Phase diagram of stable uniform solutions and domain wall solutions ($\gamma=0.55$). The phase diagram for $\gamma>1/2$ is qualitatively the same as this figure. For spatially uniform solutions, there appear two oscillations, the Ising-SRO and Ising-SBO phases, but the *XY*-type oscillation is not observed. In the Ising-SBO phase, the domain wall solution is present, and only the Néel wall is observed. For domain wall solutions, see Sec. III.

ics. This allows the spin to oscillate along the easy axis, and we observe the Ising-SBO phase. In the low frequency limit $\Omega\to 0$ with $\gamma>0$, only Ising oscillations are observed because the spin can follow the field and oscillates along the X axis. On the other hand, for $\gamma<0$, the easy axis is Y, and the XY-SRO phase is observed in a low frequency region. If h is strong enough, the spin can follow the field and the spin shows the Ising-SRO phase.

III. OSCILLATION OF MAGNETIC WALLS

In the absence of an oscillating magnetic field, below the critical temperature, domain walls appear reflecting the breaking of reversal symmetry for the local magnetization (see Appendix A). The appearance of spatial structures in connection with symmetry breaking is a universal scenario. Even in an oscillating magnetic field, several stable limit cycles can coexist in the Ising-SBO, XY-SRO, and XY-SBO phases as mentioned in Sec. II. In a spatially extended system, each of the degenerate limit cycles can freely occupy any part of the spatial region and yields domain structures,

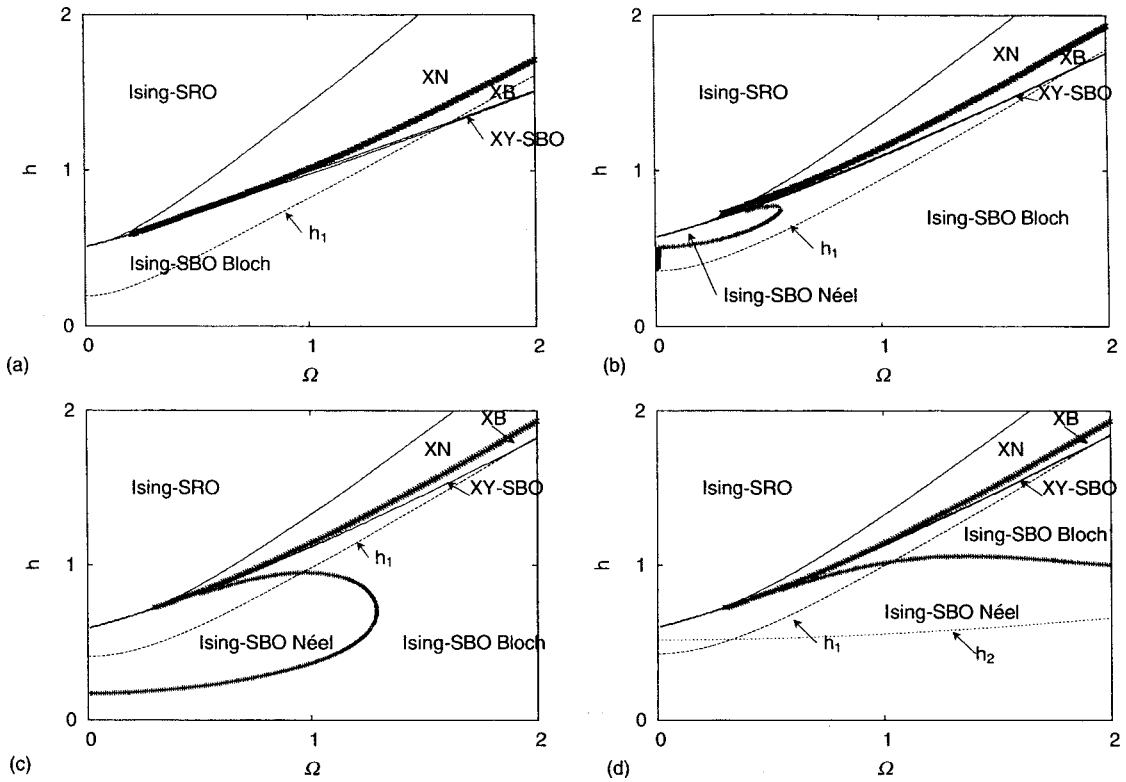

FIG. 3. Typical phase diagrams of stable uniform solutions and domain wall solutions for $0<\gamma<1/2$: (a) $\gamma=0.2$, (b) $\gamma=0.3$, (c) $\gamma=0.33$, and (d) $\gamma=0.34$. Phase diagrams represent the regions of stable uniform solutions and stable domain wall solutions for each γ. For domain wall solutions, see Sec. III. Here "XN" and "XB" denote the XY-SRO Néel and XY-SRO Bloch wall regions, respectively. Symbols denote the numerically obtained Néel-Bloch transition line, solid lines represent the transition lines for the uniform solutions obtained by the Floquet analysis, and the dotted lines stand for the Néel-Bloch transition lines obtained by the Fourier expansion approximation (see Sec. IV C). h_1 and h_2 stand for the XY-SRO Néel-Bloch transition line [Eq. (4.22)] and the Ising-SBO Néel-Bloch transition line [Eq. (4.24)], respectively. The Néel-Bloch transition in the Ising-SBO phase is observed in the region $\tilde{\gamma}<\gamma<1/2$, where $\tilde{\gamma}$ is a numerical value in $0.2<\tilde{\gamma}<0.3$. The region of the Ising-SBO Néel wall rapidly expands as γ approaches $\gamma=1/3$. In the $h=0$ case, the Bloch and Néel walls are stable, respectively, for $|\gamma|<1/3$ and $1/3<|\gamma|$. The XY-SBO phase exists in a narrow region between the XY-SRO and Ising-SBO phases.

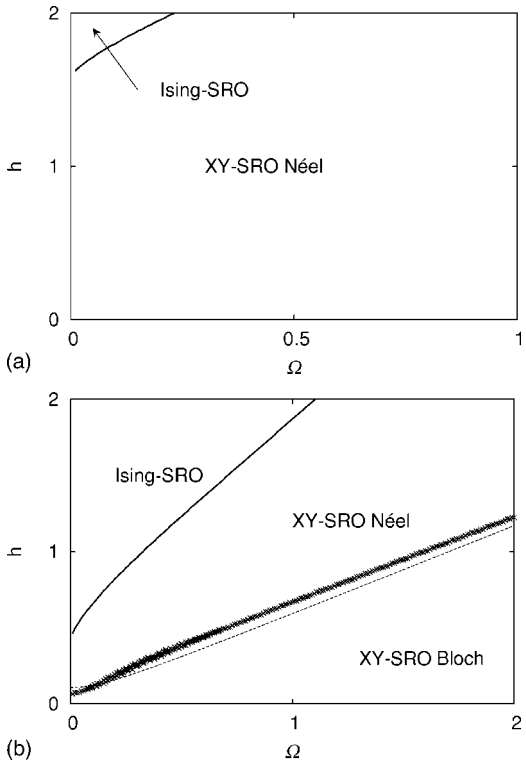

FIG. 4. Typical phase diagrams of stable uniform solutions and domain wall solutions for $\gamma<0$: (a) $\gamma=-0.4$ and (b) $\gamma=-0.05$. Phase diagrams for $\gamma<-1/3$ and $-1/3<\gamma<0$ are qualitatively the same as (a) and (b), respectively. Diagrams represent the regions of stable uniform solutions and stable domain wall solutions for each γ. For domain wall solutions, see Sec. III. Symbols denote the numerically obtained Néel-Bloch transition line, solid lines represent the transition lines for the uniform solutions obtained by the Floquet analysis, and the dotted line stands for the Néel-Bloch transition line h_1 obtained by the Fourier expansion approximation (see Sec. IV C).

and thus it is expected that certain types of domain walls exist. In this section, we discuss possible magnetic wall structures, and show that the Néel-Bloch transition is caused by local symmetry breaking as the control parameter is changed. In this paper, we will not discuss wall structures in the *XY*-SBO phase, where only the Bloch walls exist and the Néel-Bloch transition is absent.

Equation (1.3) was numerically solved by the fourth order Runge-Kutta method, by replacing $\partial_z^2 X(\partial_z^2 Y)$ with $[X(n+1)-2X(n)+X(n-1)]/(\Delta z)^2([Y(n+1)-2Y(n)+Y(n-1)]/(\Delta z)^2)$, where $X(n)$ denotes the X component at the nth lattice site at time t. We set the lattice unit $\Delta z=0.25$ and the system size $L=128$ (512 sites). This size is sufficiently larger than the width of a single magnetic wall. The time step Δt is $\Delta t=T/(2048m)$ $(m=1,2,\ldots)$, where the natural number m is taken to be the minimum value that satisfies $\Delta t<0.01$. The boundary conditions at $z=0$ and $z=L$ were chosen as $\psi(z=0,t)=\psi^{(1)}(t)$ and $\psi(z=L,t)=\psi^{(2)}(t)$, where $\psi^{(1)}(t)$ and $\psi^{(2)}(t)$ are two stable limit cycles of the uniform solutions in the Ising-SBO (*XY*-SRO) phase. In order to obtain a single wall near $z=L/2$, we set the initial conditions $\psi(z,0)=\psi^{(1)}(0)+\delta_z$ $(z\in[0,L/2])$, $\psi(z,0)=\psi^{(2)}(0)+\delta_z$ $(z\in(L/2,L])$, where the δ_z's are uniform random numbers ranging in $[-0.01,0.01]$.

We discuss the stationary periodic motion of the magnetic walls. In the Ising-SBO phase, we confirmed that there are two types of magnetic walls, the Néel and Bloch walls. Figures 5 and 6 represent the oscillation of a single Néel and Bloch wall, respectively. Due to the spatial symmetry, a single wall exhibits no drift motion. In the Ising-SBO phase, the Néel wall solution always exists because Eq. (1.3) always has the solution $Y(z,t)=0$. The local dynamics around the wall is described as Ising-SBO for the Néel wall case, and *XY*-SBO for the Bloch wall case; namely, the Néel-Bloch transition is connected with the local symmetry breaking around the wall.

In the *XY*-SRO phase, two types of wall exist, and the Néel-Bloch transition exists. The oscillation manner of the walls is slightly different from that for the Ising-SBO case. The *XY*-SRO Néel wall is defined as a wall for which the time average $\overline{X(z,t)}\equiv T^{-1}\int_t^{t+T}X(z,s)ds$ vanishes for any z and t (Fig. 7). The X component of the local dynamics is symmetric in time, i.e., the local dynamics is *XY*-SRO type. The *XY*-SRO Bloch wall is defined as a wall with $\overline{X(z,t)}\neq 0$ (Fig. 8). In this case, the local dynamics is not the complete *XY*-SRO type oscillation but the *XY*-SBO type, especially near the wall region.

IV. METHODS TO DETERMINE NÉEL-BLOCH TRANSITION POINTS

In this section we show how to determine the Néel-Bloch transition points as the control parameter h or Ω is changed. One is the determination by numerical simulation in the Ising-SBO and *XY*-SRO phases, and the other is a theoretical method with the Fourier expansion approximation.

A. Linear stability analysis of the Néel wall solution in the Ising-SBO phase

In the case that the stable uniform solution is in the Ising-SBO phase, there exists a Néel wall particular solution $(X_N(z,t),0)$. Let $(x(z,t),y(z,t))$ be a small perturbation from the Néel wall particular solution at time t. The linearized equation of motion for the deviation $y(z,t)$ is given by

$$\dot{y}(z,t)=[1-\gamma-X_N^2(z,t)+\partial_z^2]y(z,t)\equiv\hat{g}(z,t)y(z,t). \tag{4.1}$$

Only the deviation $y(z,t)$ is relevant to the stability of the Néel wall solution. The Néel wall solution $X_N(z,t)$ is a period-T function, and thus $\hat{g}(z,t)$ is a periodic operator, $\hat{g}(z,t+T)=\hat{g}(z,t)$.

It is convenient to introduce the norm $m(t)$ by

$$y(z,t)=m(t)\,\eta(z,t), \tag{4.2}$$

$$m(t)\equiv\sqrt{\frac{1}{L}\int_0^L|y(z,t)|^2dz}. \tag{4.3}$$

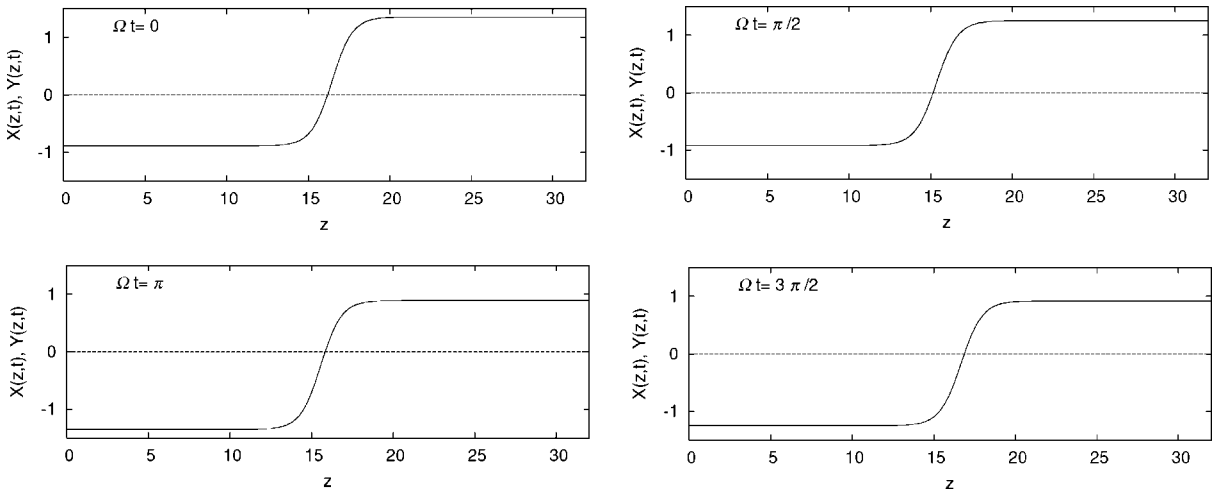

FIG. 5. Periodic oscillation of an Ising-SBO Néel wall for $\gamma=0.34$, $h=0.8$, and $\Omega=1.5$. The solid lines indicate $X(z,t)$, and the broken lines $Y(z,t)$. In the Néel wall case, $Y(z,t)$ vanishes.

Note that $\langle|\eta|^2\rangle=1$, where the angular brackets mean the spatial average $\langle A\rangle\equiv\int_0^L A(z)dz/L$. Multiplying Eq. (4.1) by η after the substitution of Eq. (4.2) into it, and taking the spatial average, we get

$$\dot{m}(t)=\Lambda(t)m(t), \tag{4.4}$$

where the expansion rate of $m(t)$ at time t is defined by

$$\Lambda(t)=\langle\eta\hat{g}\eta\rangle=1-\gamma-\langle X_N^2\eta^2\rangle+\langle\eta\partial_z^2\eta\rangle. \tag{4.5}$$

For sufficiently large t, Eq. (4.4) is solved to yield

$$m(t)\sim m(0)e^{\lambda t},\quad \lambda=\frac{1}{T}\int_0^T\Lambda(s)ds, \tag{4.6}$$

except for an oscillating prefactor in $m(t)$. The exponent λ, which is equivalent to the time average of $\Lambda(t)$, is relevant to the linear stability of the Néel wall. If $\lambda<0$, the Néel wall solution is linearly stable. On the other hand, if $\lambda>0$, the Néel wall is unstable; alternatively, the Bloch wall becomes stable. The marginal state $\lambda=0$ stands for the Néel-Bloch transition point. We confirmed by numerical experiment that $m(t)$ grows exponentially in time, and determined the Néel-Bloch transition point in the Ising-SBO phase by using λ obtained by the method of least squares.

Figure 3 shows phase diagrams for the domain wall structures in the Ising-SBO phase as well as the regions of stable uniform solutions. The Néel-Bloch transition in the Ising-SBO phase occurs in the region $\tilde{\gamma}<\gamma<1/2$, where $\tilde{\gamma}$ takes a value within $0.2<\tilde{\gamma}<0.3$. In the absence of an applied field ($h=0$), the Bloch wall is observed for $0<\gamma<1/3$ (Appendix A). As argued in Sec. II, the presence of the applied oscillating field brings a tendency to make spins parallel to the Y axis. As a result, in the region $0<\gamma<\tilde{\gamma}$ [Fig. 3(a)], the Bloch wall is observed. In the low frequency regime in $\tilde{\gamma}<\gamma<1/3$, since spins easily respond to the alternation of the magnetic field and also tend to be parallel to the X axis, the Néel wall is observed. Figure 3 shows that as γ approaches $1/3$ the region of the Néel wall rapidly expands [Figs. 3(b) and 3(c)], and that at $\gamma=1/3$ the phase diagram abruptly changes [Fig. 3(d)]. In the region $1/3<\gamma<1/2$, although the Néel wall is observed in the absence of the field, the

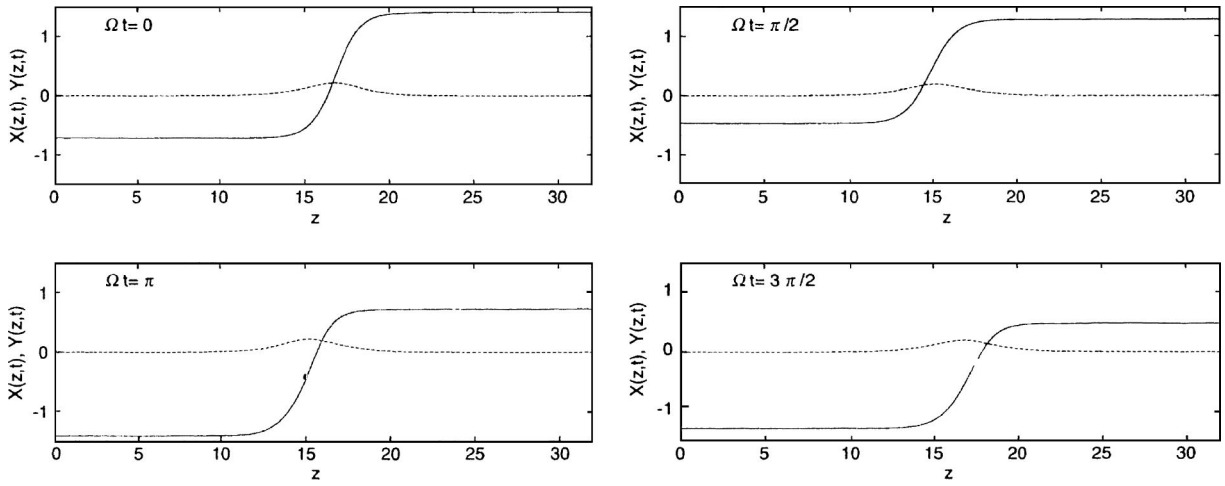

FIG. 6. Periodic oscillation of an Ising-SBO Bloch wall for $\gamma=0.34$, $h=1.2$, and $\Omega=1.5$. The setting of the graph is the same as Fig. 5. A Bloch wall has a nonvanishing Y component.

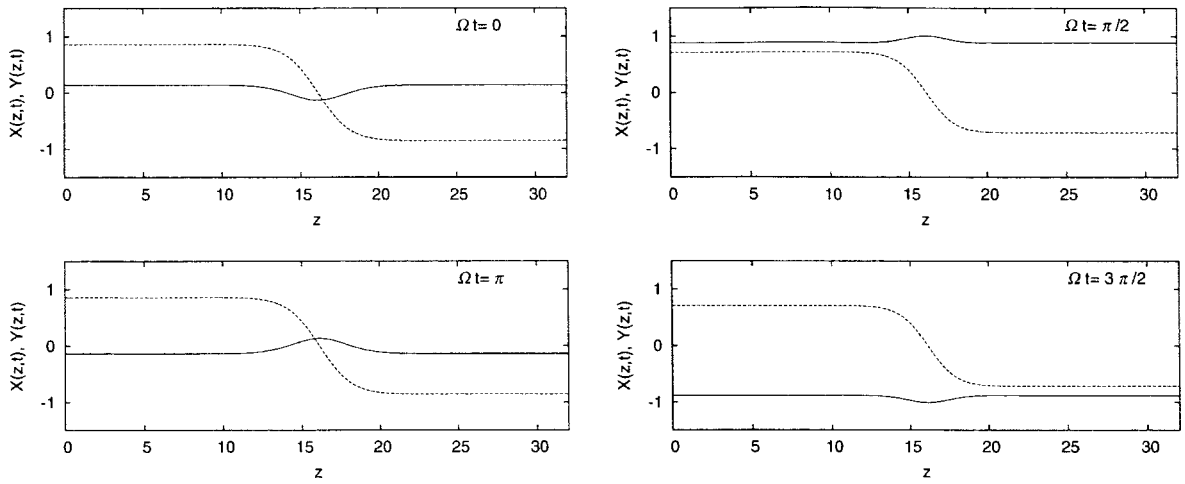

FIG. 7. Periodic oscillation of an *XY*-SRO Néel wall for $\gamma=-0.05$, $h=1.5$, and $\Omega=1.5$. The solid and broken lines indicate $X(z,t)$ and $Y(z,t)$. $\overline{X(z,t)}$ vanishes even though $X(z,t)\neq 0$ at any time.

Bloch wall stably exists because spins tend to be parallel to the Y axis as the amplitude of the field is increased. In the strong anisotropy region $\gamma>1/2$, only the Néel wall is observed, i.e., the Néel-Bloch transition does not occur.

B. Determination of the Néel-Bloch transition point in the *XY*-SRO phase

The linear stability analysis for a period-T domain wall solution in the *XY*-SRO phase is intricate compared with that in the Ising-SBO phase. Let $\psi_W(z,t)=X_W(z,t)+iY_W(z,t)$ be a magnetic wall solution in the *XY*-SRO phase, and $\delta\psi(z,t)\equiv\psi(z,t)-\psi_W(z,t)=x(z,t)+iy(z,t)$ be the deviation from that. From Eq. (1.3) the linear equation of motion for $\delta\psi(z,t)$ is written as

$$\frac{d}{dt}\begin{pmatrix}x(z,t)\\ y(z,t)\end{pmatrix}=\hat{G}(\psi_W(z,t))\begin{pmatrix}x\\ y\end{pmatrix}, \tag{4.7}$$

$$\hat{G}(\psi_W)=\begin{pmatrix}1+\gamma-3X_W^2-Y_W^2+\partial_z^2 & -2X_WY_W\\ -2X_WY_W & 1-\gamma-X_W^2-3Y_W^2+\partial_z^2\end{pmatrix}. \tag{4.8}$$

It is found that Eq. (4.7) always has a particular solution

$$\delta\psi(z,t)=\partial_z\psi_W(z,t), \tag{4.9}$$

which corresponds to the translational mode belonging to the zero eigenvalue. The translational mode is not relevant to the change of stability of wall solutions. It is therefore necessary to eliminate the zero mode from $\delta\psi$ in order to determine the Néel-Bloch transition point in the *XY*-SRO phase. This fact, however, makes a numerical scheme based on the linear stability analysis difficult because of the unavoidable error due to numerical differentiation. Avoiding this difficulty, we determine the Néel-Bloch transition point by setting a threshold value for the maximum value X_B of $\overline{|X(z,t)|}$; namely, after an initial transient process has passed, the wall type is classified as a Bloch or Néel wall by checking whether X_B is beyond or

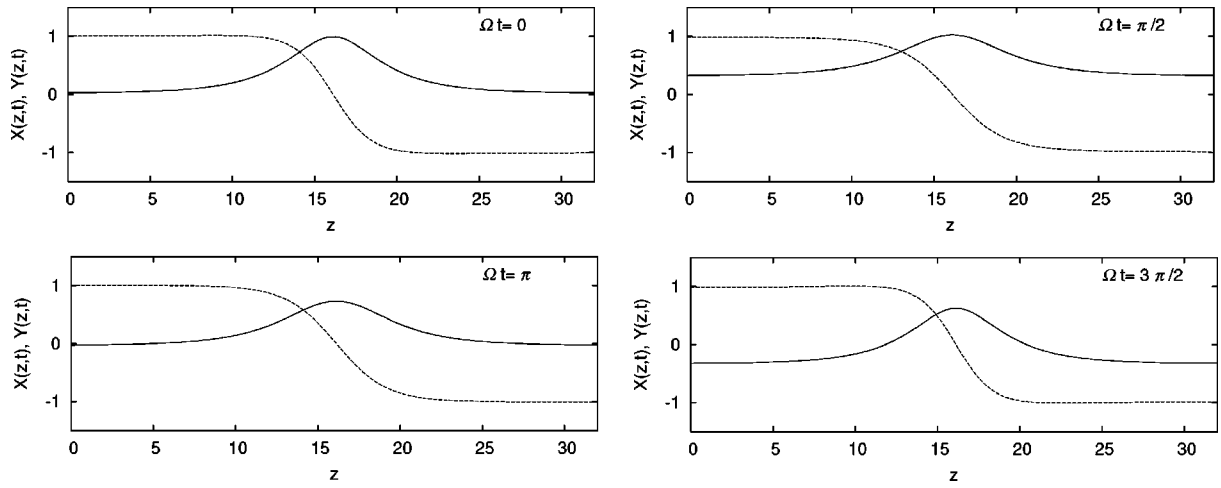

FIG. 8. Periodic oscillation of an *XY*-SRO Bloch wall for $\gamma=-0.05$, $h=0.5$, and $\Omega=1.5$. The setting of the graph is the same as Fig. 7. $\overline{X(z,t)}$ does not vanish in the wall region.

below the given threshold value, which was set to be 10^{-3}. As will be shown in Sec. V, a hysteresis may be present at the Néel-Bloch transition point for certain parameter regions. In this case, we obtained phase diagrams through the estimation of the transition point for both cases of increasing and decreasing h per one fixed value of Ω.

In the XY-SRO phase, the Néel-Bloch structure transition exists for $-1/3<\gamma<1/2$. The phase diagrams are shown in Figs. 3 and 4. In the region $\gamma<-1/3$ [Fig. 4(a)], only the Néel wall is observed. When the Néel-Bloch transition exists, Néel and Bloch walls are observed, respectively, for the high and low amplitude regimes of applied field. The Néel-Bloch transition accompanies the symmetry breaking as described in the previous section.

C. Determination of the Néel-Bloch transition point with Fourier expansion method and comparison with numerical experiment

In this subsection an analytical method to determine the Néel-Bloch transition point is developed. By using the Fourier expansion with the fundamental frequency Ω of the applied field, $X(z,t)$ and $Y(z,t)$ are expanded as follows:

$$X(z,t)=\sum_{n=-\infty}^{\infty}X_n(z,t)e^{in\Omega t},\ Y(z,t)=\sum_{n=-\infty}^{\infty}Y_n(z,t)e^{in\Omega t}. \tag{4.10}$$

Since X and Y are real, we get $X_n^*=X_{-n}$ and $Y_n^*=Y_{-n}$. Let us assume that the time scale of the variation of the coefficients $\{X_n\}$ and $\{Y_n\}$ is sufficiently longer than the period $T(=2\pi/\Omega)$ of the oscillating field. Substituting the series of expansion into Eq. (1.3), we obtain the equations of motion for the Fourier coefficients $\{X_n\}$ and $\{Y_n\}$ [13]. In this article, we use a truncation approximation keeping only the terms including the coefficients for harmonics $n\Omega(n=0,\ \pm1)$. Furthermore, we use the approximation for X_1 and Y_1 that they are regarded to be spatially homogeneous and stationary. The detailed derivation is shown in Appendix B. Using the complex variable $\psi_0(z)=X_0(z)+iY_0(z)$, the equation for the stationary state is obtained as

$$0=c_0\psi_0-|\psi_0|^2\psi_0+\gamma_0\psi_0^*+\partial_z^2\psi_0, \tag{4.11}$$

$$c_0=1-4|X_1|^2, \tag{4.12}$$

$$\gamma_0=\gamma-2|X_1|^2 \tag{4.13}$$

for the situation in which the stable uniform solutions are in the Ising-SBO phase or the XY-SRO phase. This is just the same form as Eq. (A1) for the stationary state without an oscillating field. Now let us find a single domain wall solution under the boundary conditions $X_0(z)|_{z\to\pm\infty}=X_0^{\pm}$ and $Y_0(z)|_{z\to\pm\infty}=Y_0^{\pm}$. $X_0^{\pm}$ and $Y_0^{\pm}$ are the two stable uniform solutions of $X_0(z)$ and $Y_0(z)$ (Appendix B). One should note that X_1 is the solution of the equation

$$X_1=-\frac{he^{i\tan^{-1}(\Omega/A)}}{2\sqrt{\Omega^2+A^2}}, \tag{4.14}$$

$$A=1+\gamma-3|X_0^+|^2-|Y_0^+|^2-3|X_1|^2. \tag{4.15}$$

In the Ising-SBO phase, one obtains $(X_0^+)^2=(X_0^-)^2=1+\gamma-6|X_1|^2$, $Y_0^{\pm}=0$, $X_1\neq0$, and $Y_1=0$. In the XY-SRO phase, the relations $X_0^{\pm}=0$, $(Y_0^+)^2=(Y_0^-)^2=1-\gamma-2|X_1|^2$, $X_1\neq0$, and $Y_1=0$ hold (Appendix B). The averaging procedure of the effect due to the oscillating field renormalizes the coefficients c_0 and γ_0. c_0 and γ_0 may be regarded to be an effective reduced temperature and an effective magnitude of anisotropy, respectively. From Eqs. (4.12) and (4.13) and the conditions for each of coefficients, for both the Ising-SBO and the XY-SRO phases, one finds $c_0<1$ and $\gamma_0<\gamma$. These facts may be interpreted as that the oscillating field raises the effective temperature and reduces the magnitude of the anisotropy.

Depending on the magnitude of the renormalized anisotropy parameter γ_0, the stationary solution of Eq. (4.11) is obtained as follows. For the case $\gamma_0>c_0/3$, the Ising-SBO Néel wall solution

$$X_0(z)=\pm\sqrt{c_0+|\gamma_0|}\tanh[z\sqrt{(c_0+|\gamma_0|)/2}],\ Y_0(z)=0, \tag{4.16}$$

is stable. For the case $0<\gamma_0<c_0/3$, the Ising-SBO Bloch wall solution

$$X_0(z)=pX_0^{IB}\tanh(z/\xi_{IB}),$$

$$Y_0(z)=qY_0^{IB}\,\mathrm{sech}(z/\xi_{IB}) \tag{4.17}$$

is stable, where $X_0^{IB}=\sqrt{c_0+|\gamma_0|}$, $Y_0^{IB}=\sqrt{c_0-3|\gamma_0|}$, and $\xi_{IB}=1/\sqrt{2|\gamma_0|}$. p and q take values of $+1$ or -1. For the case $-c_0/3<\gamma_0<0$, the XY-SRO Bloch wall solution

$$X_0(z)=pX_0^{XB}\,\mathrm{sech}(z/\xi_{XB}),$$

$$Y_0(z)=qY_0^{XB}\tanh(z/\xi_{XB}) \tag{4.18}$$

is stable, where $X_0^{XB}=\sqrt{c_0-3|\gamma_0|}$, $Y_0^{XB}=\sqrt{c_0+|\gamma_0|}$, and $\xi_{XB}=1/\sqrt{2|\gamma_0|}$. For the case $\gamma_0<-c_0/3$, the XY-SRO Néel wall solution

$$Y_0(z)=\pm\sqrt{c_0+|\gamma_0|}\tanh[z\sqrt{(c_0+|\gamma_0|)/2}],\ X_0(z)=0, \tag{4.19}$$

is stable.

At the Néel-Bloch transition point, the relation $|\gamma_0|=c_0/3$ holds. By using Eqs. (4.12) and (4.13), this relation is rewritten as

$$\left|\gamma-2|X_1|^2\right|=\frac{1-4|X_1|^2}{3}. \tag{4.20}$$

In the following, we deal with the two cases according to the sign of γ_0.

(1) $\gamma_0=\gamma-2|X_1|^2<0$. This case concerns the domain wall solutions in the XY-SRO phase. The solution of Eq. (4.20) is given by

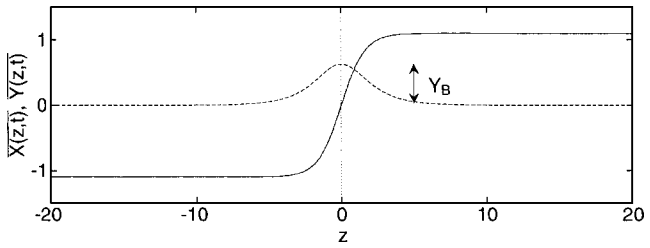

FIG. 9. A schematic figure of the modulus of the Bloch wall. The solid line indicates $\overline{X(z,t)}$, and the broken line indicates $\overline{Y(z,t)}$. The above figure corresponds to the Ising-SBO case, where Y_B is the modulus of the Bloch wall. In the *XY*-SRO case, the modulus X_B is the peak value of $\overline{X(z,t)}$.

$$|X_1|^2 = \frac{3}{10}\left(\frac{1}{3} + \gamma\right). \tag{4.21}$$

The condition $\gamma - 2|X_1|^2 < 0$ is then reduced to $\gamma < 1/2$. Additionally $1+3\gamma > 0$ must hold from Eq. (4.21). The *XY*-SRO Néel-Bloch transition is, therefore, allowed in the region $-1/3 < \gamma < 1/2$. Substituting Eq. (4.21) into the modulus of Eq. (4.14), we obtain the Néel-Bloch transition point $h = h_1(\Omega)$, where

$$h_1(\Omega) = \sqrt{\frac{6}{5}\left(\frac{1}{3} + \gamma\right)\left(\Omega^2 + \frac{(17\gamma - 1)^2}{100}\right)}. \tag{4.22}$$

(2) $\gamma_0 > 0$. This case concerns the domain wall solutions in the Ising-SBO phase. The solution of Eq. (4.20) is given by

$$|X_1|^2 = \frac{3}{2}\left(\gamma - \frac{1}{3}\right). \tag{4.23}$$

The condition $\gamma_0 > 0$ combined with Eq. (4.23) leads to the result that the Ising-SBO Néel-Bloch transition is allowed in the region $1/3 < \gamma < 1/2$. Substituting Eq. (4.23) into the modulus of Eq. (4.14), we obtain the Néel-Bloch transition point $h = h_2(\Omega)$, where

$$h_2 = \sqrt{6\left(\gamma - \frac{1}{3}\right)\left(\Omega^2 + \frac{(41\gamma - 19)^2}{4}\right)}. \tag{4.24}$$

Figures 3 and 4 show the Néel-Bloch transition curves obtained both theoretically and numerically. The Fourier expansion approximation mentioned above leads to the result that the Néel-Bloch transition does not appear in the region $0 < \gamma < 1/3$. Although the theoretical result for the transition lines based on the present simply truncated Fourier expansion yields a qualitatively same result to the numerical experiments in the high frequency region, the theoretical result disagrees with the numerical experiment in the low frequency regime. This is because, in the present approximation, the Fourier expansion takes into account only the terms until the first order of Ω, which is not applicable for the low frequency regime, where higher order harmonics become effective.

The Néel-Bloch transition point in the *XY*-SRO phase is close to the prediction of the present Fourier expansion approximation. Since in the *XY*-SRO phase the movement of the wall center is inconspicuous (see Figs. 7 and 8), higher order harmonics give no dominant contribution. This may be the reason why the present treatment works well.

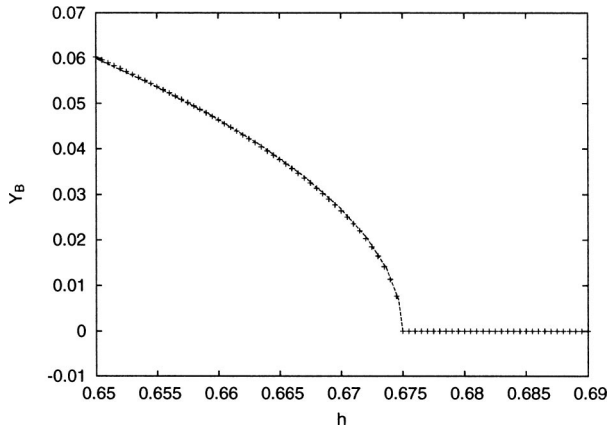

FIG. 10. The relation between h and $Y_B(h)$ around the Ising-SBO Néel-Bloch transition point ($h = h_2$). The parameter values are $\gamma = 0.3$ and $\Omega = 0.5$. The symbols and solid line represent the numerical result and the function form $Y_B = 0.379\sqrt{0.675 - h}$.

V. CRITICAL BEHAVIOR OF THE BLOCH WALL MODULUS AROUND THE NÉEL-BLOCH TRANSITION POINT

In order to characterize the Néel-Bloch transition in the oscillating magnetic field, we study the h dependence of the modulus of the Bloch wall at the neighborhood of the Néel-Bloch transition point. The modulus of the Bloch wall Y_B (X_B) in the Ising-SBO (*XY*-SRO) phase is defined as the maximum of the period average of the Y (X) component (Fig. 9).

A. Numerical results

Figure 10 shows the numerical result for the h depen-

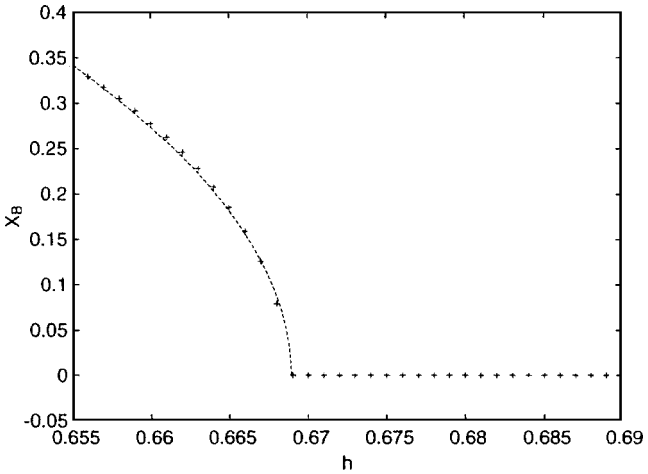

FIG. 11. The relation between h and $X_B(h)$ around the *XY*-SRO Néel-Bloch transition point ($h = h_1$). Parameter values are $\gamma = -0.05$ and $\Omega = 1.0$. The symbols and broken line represent the numerical results and the function form $X_B = 2.90\sqrt{0.6689 - h}$. The Néel-Bloch transition is continuous, and the relation $X_B \propto \sqrt{h_1 - h}$ holds below the transition point.

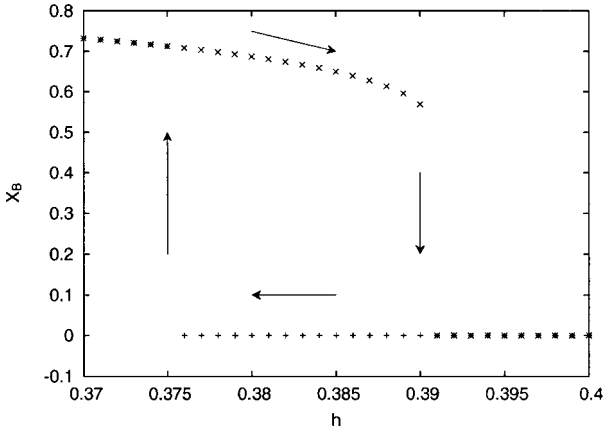

FIG. 12. The relation between h and $X_B(h)$ around the XY-SRO Néel-Bloch transition point, when $\gamma=-0.05$ and $\Omega=0.5$. The symbols + (×) indicates the numerical results for h being varied downward (upward). The result shows a hysteresis, and therefore the Néel-Bloch transition is the first order transition.

dence of the modulus of the Bloch wall in the Ising-SBO phase for a fixed Ω. It reveals that Y_B behaves as

$$Y_B(h) \propto \sqrt{|h-h_2|} \tag{5.1}$$

around the Néel-Bloch transition point ($h=h_2$). When $\gamma>1/3$($\gamma<1/3$), the Bloch wall appears above (below) h_2. In this case no hysteresis is observed.

In the XY-SRO case, below the Néel-Bloch transition point ($h=h_1$) the modulus of the Bloch wall is also scaled as $X_B \propto \sqrt{h_1-h}$ almost always for a large Ω (Fig. 11). However, we observed a hysteresis near the transition point in a narrow region for $\gamma \leqslant 0$ when Ω is small (Fig. 12). This fact shows that in this case the transition is discontinuous.

B. Theoretical analysis

In order to analyze the critical behavior of the modulus of the Bloch wall, we apply the Fourier expansion analysis. Since the modulus Y_B of the Ising-SBO Bloch wall corresponds to Y_0^{IB} in Eq. (4.17), we get

$$Y_B = \sqrt{c_0 - 3|\gamma_0|} = \sqrt{1-3\gamma+2|X_1|^2}, \tag{5.2}$$

$$c_0 = 1-4|X_1|^2,\ \gamma_0 = \gamma - 2|X_1|^2 > 0.$$

The modulus X_B of the XY-SRO Bloch wall corresponds to X_0^{XB} in Eq. (4.18), we obtain

$$X_B = \sqrt{c_0 - 3|\gamma_0|} = \sqrt{1+3\gamma-10|X_1|^2}, \tag{5.3}$$

$$c_0 = 1-4|X_1|^2,\ \gamma_0 = \gamma - 2|X_1|^2 < 0.$$

If $c_0-3|\gamma_0|<0$, no Bloch wall solution exists and the possible wall is the Néel wall. Therefore, the Néel-Bloch transition point is determined by the condition $c_0=3|\gamma_0|$. In the Ising-SBO phase, the Néel-Bloch transition is continuous when Y_B changes continuously with h, i.e., $(\partial/\partial h)(c_0-3|\gamma_0|)|_{h=h_2}$ exists. If we expand Y_B^2 around the transition point ($h=h_2$) as

$$Y_B^2 = (c_0-3|\gamma_0|)|_{h=h_2} + \frac{\partial}{\partial h}(c_0-3|\gamma_0|)|_{h=h_2}(h-h_2) + \cdots, \tag{5.4}$$

the first term in the right-hand side (RHS) vanishes, and we find

$$Y_B \propto \sqrt{|h-h_2|}, \tag{5.5}$$

to the lowest order in $|h-h_2|$, provided that the coefficient in the second term in the RHS is a positive definite value. In the same way, we can show that $X_B \propto \sqrt{|h-h_1|}$ near the XY-SRO Néel-Bloch transition point, if the transition is continuous. On the other hand, for the case that the transition is discontinuous as shown in Fig. 12, the above-mentioned argument should be revised. In the same line as the expansion Eq. (5.4), we supposed that the discontinuity of the transition was due to h being a nonmonotonic function of $|X_1|^2$. Note that $c_0-3|\gamma_0|$ is a function of $|X_1|^2$, and that h and $|X_1|^2$ are related to the modulus squared of Eq. (4.14). However such a nonmonotonic behavior of h could not be proved; this may depend on the present approximation, and the problem remains unsolved. This suggests that we need to take the spatial variation of the Fourier coefficients other than the 0th order or further higher harmonics of those into account in order to obtain more reliable expressions of X_B and X_1.

Applying the Landau expansion, we can also show the scaling near the Ising-SBO Néel-Bloch transition point. In the present case the Y component is relevant to the critical behavior. The perturbation $\mathbf{(}0,y(z,t)\mathbf{)}$ from the Néel wall structure concerns the stability of the Néel wall solution $\mathbf{(}X_N(z,t),0\mathbf{)}$ near the transition point. The time evolution of $y(z,t)$ becomes

$$\dot{y}(z,t) = [1-\gamma-X_N^2(z,t)+\partial_z^2]y - y^3. \tag{5.6}$$

The solution of Eq. (5.6) can be formally written as

$$y(z,t) = U(z,t)y(z,0), \tag{5.7}$$

$$U(z,t) = \exp_+\left(\int_0^t ds[1-\gamma-X_N^2(z,s)+\partial_z^2]\right) \equiv Q(z,t)e^{t\Lambda(z)}, \tag{5.8}$$

where $\exp_+[\cdots]$ is the time ordered exponential and $Q(z,t)$ is a period-T operator, i.e., $Q(z,t+T)=Q(z,t)$, due to the Floquet theorem. $\Lambda(z)$ is the Floquet operator defined by $U(z,t)=e^{T\Lambda(z)}$. Rewriting $y(z,t)$ as $y(z,t)=Q(z,t)\tilde{y}(z,t)$ and substituting this expression into Eq. (5.6), we get

$$\dot{\tilde{y}}(z,t) = \Lambda(z)\tilde{y} - [Q(z,t)]^{-1}(Q\tilde{y})^3. \tag{5.9}$$

Expanding $\tilde{y}$ as $\tilde{y}=\Sigma_\alpha a_\alpha(t)\phi_\alpha(z)$ by using the eigenfunctions $\phi_\alpha(z)$ of $\Lambda(z)$ and retaining only the coefficient corresponding to the largest eigenvalue ($\alpha=0$), we obtain

$$\dot{a}_0(t) \simeq \lambda_0 a_0(t) - c(t)[a_0(t)]^3, \tag{5.10}$$

where $c(t)$ is a period-T function. The numerical results imply that $\lambda_0 \sim h_2-h$ near $h=h_2$. Applying the averaging pro-

cedure for $c(t)$ over one period, the stationary solution for $a_0(t)$ is obtained as

$$a_0^{st} = \sqrt{\frac{\lambda_0}{\bar{c}}} \propto \sqrt{|h - h_2|}, \tag{5.11}$$

where $\bar{c}$ is assumed to be positive. This result gives the scaling $Y_B \sim |h - h_2|^{1/2}$.

VI. SUMMARY AND CONCLUDING REMARKS

In the present paper, we studied the magnetic wall structures of the 1D anisotropic *XY*-spin system under an oscillating magnetic field by making use of the Ginzburg-Landau model from the nonlinear mechanical viewpoint, particularly the wall structures in the Ising-SBO and *XY*-SRO phases. It was numerically shown that there exist two types of walls, i.e., the Néel and Bloch walls, and that there exists a transition between the states where the Néel wall and Bloch wall stably exist as either the amplitude or the frequency of the applied field is changed.

We observed the phase diagram for the stable wall structures spanned by the amplitude and the frequency of the external field. We found that the Ising-SBO Néel wall and Ising-SBO Bloch wall are stable, respectively, for $\tilde{\gamma} < \gamma$, $\tilde{\gamma}$ being a value in between 0.2 and 0.3, and $0 < \gamma < 1/2$ and that the *XY*-SRO Néel wall and the *XY*-SRO Bloch wall are stable respectively for $\gamma < 1/2$ and $-1/3 < \gamma < 1/2$. Furthermore, we compared these results with those of the Fourier expansion analysis. The qualitative agreement on the Néel-Bloch transition is quite good for the *XY*-SRO phase. However, the analysis was incapable of explaining the appearance of the Néel wall in the low frequency region for $\tilde{\gamma} < \gamma < 1/3$ associated with the Ising-SBO Néel-Bloch transition.

Furthermore, we showed that the Néel-Bloch transition can be either continuous or discontinuous depending on the value of the frequency of the applied magnetic field. When the transition is continuous, the numerical simulation shows that the modulus of the Bloch wall is scaled as the square root of the deviation from the critical value of control parameter. It was shown that this result is capable of being explained by making use of the Fourier expansion analysis.

ACKNOWLEDGMENTS

The present study was partially supported by Grant-in-Aid for Scientific Research (C) of the Ministry of Education, Culture, Sports, Science and Technology, and the 21st Century COE program "Center of Excellence for Research and Education on Complex Functional Mechanical Systems" at Kyoto University.

APPENDIX A: MAGNETIC WALL (NÉEL AND BLOCH) STRUCTURES IN THE ABSENCE OF FIELD

This section briefly reviews domain wall solutions of the TDGL equation below the critical temperature in the absence of the applied field,

$$\dot{\psi}(z,t) = \psi - |\psi|^2\psi + \gamma\psi^* + \partial_z^2\psi = -\frac{\delta\mathcal{H}}{\delta\psi^*}. \tag{A1}$$

Here $\mathcal{H}$ is the Landau free energy

$$\mathcal{H} = \int \left(-|\psi|^2 + \frac{1}{2}(|\psi|^2)^2 - \frac{\gamma}{2}(\psi^2 + \psi^{*2}) + |\partial_z\psi|^2 \right) dz, \tag{A2}$$

and is also a Lyapunov function. In terms of real and imaginary parts, Eq. (A1) is rewritten as

$$\dot{X}(z,t) = [1 + \gamma - (X^2 + Y^2)]X + \partial_z^2 X, \tag{A3}$$

$$\dot{Y}(z,t) = [1 - \gamma - (X^2 + Y^2)]Y + \partial_z^2 Y. \tag{A4}$$

This set of equations is invariant under the transformation $\gamma \to -\gamma$ followed by the change of the role of the components X and Y. Therefore we restrict γ to be positive without loss of generality in this appendix.

The stable uniform solutions $\mathbf{X}^{ss}$ of Eqs. (A3) and (A4) are

$$\mathbf{X}^{ss} = \begin{cases} (\pm\sqrt{1+\gamma}, 0) & (\gamma > 0), \\ (\cos\theta_0, \sin\theta_0) \quad (\theta_0 \text{ arbitrary}) & (\gamma = 0), \end{cases} \tag{A5}$$

i.e., for $\gamma \neq 0$ there are two stable uniform solutions with reversal symmetry. These symmetric states cause domain wall structures in the spatially extended system. In a 1D system, it is well known that two types of wall solution appear depending on the degree of anisotropy. The analytical expressions for those walls are given by solving Eqs. (A3) and (A4) with the boundary conditions $(X,Y) \to (\pm\sqrt{1+\gamma}, 0)$ for $z \to \pm\infty$. For $\gamma > 1/3$, the stable domain wall is the so-called Néel wall, and is given by

$$X^N(z) = \pm\sqrt{1+\gamma}\tanh\left(\sqrt{\frac{1+\gamma}{2}}(z - z_0)\right), \quad Y^N(z) = 0. \tag{A6}$$

The Néel wall solution has only one nonvanishing component. Here z_0 is the position of the wall. For $0 < \gamma < 1/3$, the stable domain wall is the so-called Bloch wall, and is given by

$$X^B(z) = p\sqrt{1+\gamma}\tanh[\sqrt{2\gamma}(z - z_0)], \tag{A7}$$

$$Y^B(z) = q\sqrt{1-3\gamma}\,\mathrm{sech}[\sqrt{2\gamma}(z - z_0)], \tag{A8}$$

where p and q take values of either $+1$ or -1. The combinations $(p,q) = (+1,+1)$ and $(-1,-1)$ are energetically equivalent. The Bloch wall has two components around the boundary of different domains. Figure 13 represents these two types of solution.

In the Bloch wall, for one sign (p) of function X^B, there are two different walls with two opposite signs (q) of function Y^B. These correspond to two opposite (right and left) rotations of spins along the z axis, and the so-called chirality, which is quantified by q/p (see Fig. 13).

The qualitative reason for the Néel-Bloch transition as the anisotropy parameter is changed is the following. The Lan-

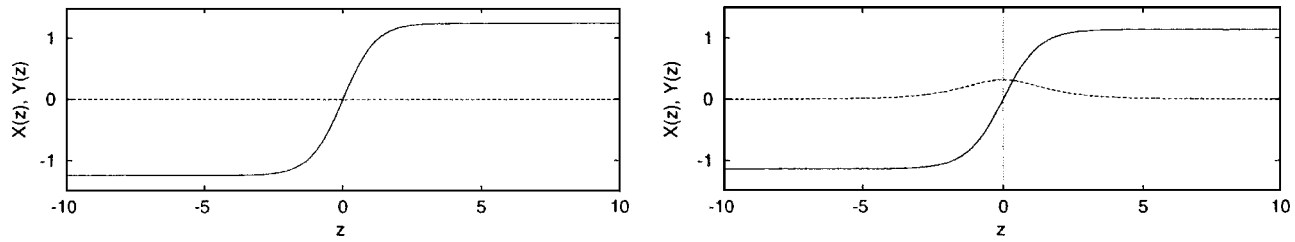

FIG. 13. Néel (left) and Bloch (right) walls in the absence of an applied field. The horizontal axis is the spatial coordinate z, and the solid and dotted lines represent X and Y components of the wall solutions, respectively. For the Néel wall, the Y component vanishes but for the Bloch wall it is present. The Bloch wall structure corresponds to the case for $p=1$ and $q=1$ [see Eq. (A8)] with the chirality $q/p=1$.

dau free energy Eq. (A2) has the anisotropy energy term $\gamma(\psi^2+\psi^{*2})/2$, which is minimized when the spins are parallel to an easy magnetization axis and, thereby, has the effect of a tendency to form a Néel wall structure. On the other hand, the term $|\partial_z\psi|^2$ has the effect of smoothing the spatial variation of the rotation angle of spins (twist), and has the effect of a tendency to form a Bloch wall structure. The Néel-Bloch transition results from the competition of these effects.

APPENDIX B: EQUATIONS OF MOTION FOR FOURIER COEFFICIENTS

In this section, we give a brief summary of the reduced equations of motion for the Fourier coefficients obtained in the Fourier expansion approximation introduced in Ref. [13]. Substituting the Fourier expansion Eq. (4.10) into the TDGL equation (1.3), the time evolution of $X_n(z,t)$ and $Y_n(z,t)$ is written as

$$\dot{X}_n + in\Omega X_n = (1+\gamma)X_n - \sum_{n_1,n_2} X_{n_1}X_{n_2}X_{n-n_1-n_2} - \sum_{n_1,n_2} Y_{n_1}Y_{n_2}X_{n-n_1-n_2} + \partial_z^2 X_n + \frac{h}{2}(\delta_{n,1}+\delta_{n,-1}), \tag{B1}$$

$$\dot{Y}_n + in\Omega Y_n = (1-\gamma)Y_n - \sum_{n_1,n_2} Y_{n_1}Y_{n_2}Y_{n-n_1-n_2} - \sum_{n_1,n_2} X_{n_1}X_{n_2}Y_{n-n_1-n_2} + \partial_z^2 Y_n. \tag{B2}$$

For the sake of simplicity, we retain only the harmonics $n=0,\pm1$, and neglect spatial variation of X_1 and Y_1, where both variables X_0^2 and Y_0^2 appearing in the equations for X_1 and Y_1 are replaced by their stable uniform solutions. For the Ising-SBO and XY-SRO phases, there are two stable limit cycle uniform solutions with broken symmetry, and we represent their 0th Fourier coefficients as $X_0^{\pm}$ and $Y_0^{\pm}$ (the signs $\pm$ denote the two broken symmetric states). For the Ising-SBO phase, the symmetry of oscillation yields $X_0^- = -X_0^+$, $Y_0^{\pm}=0$, and $Y_1=0$. For the XY-SRO phase, it yields $X_0^{\pm}=0$, $Y_0^- = -Y_0^+$ and $Y_1=0$. By using these facts, the equations of motion for X_0, Y_0, and X_1 are written as

$$\dot{X}_0(z,t) = [1+\gamma-6|X_1|^2-(X_0^2+Y_0^2)]X_0 + \partial_z^2 X_0, \tag{B3}$$

$$\dot{Y}_0(z,t) = [1-\gamma-2|X_1|^2-(Y_0^2+X_0^2)]Y_0 + \partial_z^2 Y_0, \tag{B4}$$

$$\dot{X}_1(t) + i\Omega X_1 = [1+\gamma-3(X_0^+)^2-(Y_0^+)^2-3|X_1|^2]X_1 + \frac{h}{2}. \tag{B5}$$

The Fourier coefficients $X_0^{\pm}$ and $Y_0^{\pm}$ can be obtained as the stationary uniform solutions of Eqs. (B3) and (B4). In the Ising-SBO phase, from the stable uniform solutions of Eq. (B3) with $X_0\neq0$ and $Y_0=0$, we have the relation $(X_0^{\pm})^2=1+\gamma-6|X_1|^2$. On the other hand, in the XY-SRO phase, from the stable uniform solutions of Eq. (B4) with $X_0=0$ and $Y_0\neq0$, we also have the relation $(Y_0^{\pm})^2=1-\gamma-2|X_1|^2$. The stationary equation for Eqs. (B3) and (B4) leads to Eq. (4.11), and that for Eq. (B5) yields Eq. (4.14).

[1] T. Tomé and M. J. de Oliveira, Phys. Rev. A **41**, 4251 (1990).
[2] J. F. F. Mendes and E. J. S. Lage, J. Stat. Phys. **64**, 653 (1991).
[3] S. W. Sides, P. A. Rikvold, and M. A. Novotny, Phys. Rev. Lett. **81**, 834 (1998); S. W. Sides, P. A. Rikvold, and M. A. Novotny, Phys. Rev. E **59**, 2710 (1999); G. Korniss, C. J. White, P. A. Rikvold, and M. A. Novotny, *ibid.* **63**, 016120 (2000).
[4] B. K. Chakrabarti and M. Achryya, Rev. Mod. Phys. **71**, 847 (1999).
[5] G. Korniss, P. A. Rikvold, and M. A. Novotny, Phys. Rev. E **66**, 056127 (2002).
[6] A. Chatterjee and B. K. Chakrabarti, Phys. Rev. E **67**, 046113 (2003).
[7] Q. Jiang, H.-N. Yang, and G.-C. Wang, Phys. Rev. B **52**, 14911 (1995).
[8] J.-S. Suen and J. L. Erskine, Phys. Rev. Lett. **78**, 3567 (1997).
[9] J.-S. Suen, M. H. Lee, G. Teeter, and J. L. Erskine, Phys. Rev. B **59**, 4249 (1999).

[10] H. Fujisaka, H. Tutu, and P. A. Rikvold, Phys. Rev. E **63**, 036109 (2001).
[11] H. Jang and M. J. Grimson, Phys. Rev. E **63**, 066119 (2001); H. Jang, M. J. Grimson, and C. K. Hall, Phys. Rev. B **67**, 094411 (2003); Phys. Rev. E **68**, 046115 (2003).
[12] M. Acharyya, Int. J. Mod. Phys. C **14**, 49 (2003).
[13] T. Yasui, H. Tutu, M. Yamamoto, and H. Fujisaka, Phys. Rev. E **66**, 036123 (2002); **67**, 019901(E) (2003).
[14] T. Nagai and K. Kawasaki, Physica A **120**, 587 (1983).
[15] K. Kawasaki and T. Nagai, Physica A **121**, 175 (1986).
[16] H. Tutu and H. Fujisaka, Phys. Rev. B **50**, 9274 (1994).
[17] H. Tutu, Phys. Rev. E **67**, 036112 (2003).
[18] G. J. de Valcárcel, I. Pérez-Arjona, and E. Roldán, Phys. Rev. Lett. **89**, 164101 (2002).
[19] V. Zharnitsky, I. Mitkov, and M. Levi, Phys. Rev. B **57**, 5033 (1998).
[20] A. S. Kirakosyan, F. Kh. Abdullaev, and R. M. Galimzyanov, Phys. Rev. B **65**, 094411 (2002).